

Suzaku Observation of Group of Galaxies NGC 507: Temperature and Metal Distributions in the Intra-cluster Medium

Kosuke SATO,^{1,2} Kyoko MATSUSHITA,¹ Yoshitaka ISHISAKI,³ Noriko Y. YAMASAKI,⁴
Manabu ISHIDA,⁴ and Takaya OHASHI,³

¹ *Department of Physics, Tokyo University of Science, 1-3 Kagurazaka, Shinjuku-ku, Tokyo 162-8601*

² *Graduate School of Natural Science and Technology, Kanazawa University, Kakuma, Kanazawa, Ishikawa 920-1192*
ksato@astro.s.kanazawa-u.ac.jp

³ *Department of Physics, Tokyo Metropolitan University, 1-1 Minami-Osawa, Hachioji, Tokyo 192-0397*

⁴ *Institute of Space and Astronautical Science (ISAS), Japan Aerospace Exploration Agency,
3-1-1 Yoshinodai, Sagami-hara, Kanagawa 229-8510*

(Received 2008 March 10; accepted 2008 May 14)

Abstract

Temperature and abundance distributions of the intra-cluster medium (ICM) in the NGC 507 group of galaxies were studied with Suzaku. Observed concentric annular spectra were well-represented by a two temperature model for ICM, and we found steeper abundance gradients for Mg, Si, S, and Fe compared with O in the central region. Abundance ratios of α -elements to iron were found to be similar to those in other groups and poor clusters. We calculated metal mass-to-light ratios for Fe, O and Mg (IMLR, OMLR, MMLR) for NGC 507, and values for different systems were compared. Hotter and richer systems tend to show higher values of IMLR, OMLR, and MMLR. OMLR and MMLR were measured to an outer region for the first time with Suzaku, while IMLR was consistent with that with ASCA. We also looked into 2-dimensional map of the hardness ratio, but found no significant deviation from the circular symmetry.

Key words: galaxies: clusters: individual (NGC 507), galaxies: intergalactic medium, galaxies: abundances

1. Introduction

Recent X-ray observations have shown metal abundance profiles in the ICM based on the spatially resolved spectra. Groups of galaxies carry important information about the entire history of cosmic chemical evolution, since the groups contain 50–70% of galaxies in the universe (e.g. Mulchaey et al. 2006) and they serve as building blocks of clusters of galaxies. In order to know how the ICM has been enriched, we need to measure the amount and distribution of metals in the ICM. Because Si and Fe are both synthesized in type Ia and type II supernovae (SNe Ia and II), we need to know O and Mg abundances, which are synthesized practically in SNe II, in resolving the past metal enrichment process in ICM by supernovae in early-type galaxies (Arnaud et al. 1992; Renzini et al. 1993). Comparison of the ICM properties between groups and clusters of galaxies will also enable us to understand the bottom-up process of the hierarchical structure formation in the universe.

ASCA measured the distribution of the heavy elements, such as Si and Fe, in the ICM (Fukazawa et al. 1998; Fukazawa et al. 2000; Finoguenov et al. 2000; Finoguenov et al. 2001). Renzini (1997) and Makishima et al. (2001) summarized iron-mass-to-light ratios (IMLR) for various objects, as a function of their plasma temperature serving as a measure of the system richness with ASCA, and

they showed that the early-type galaxies released large amount of metals formed through past supernovae explosions as shown earlier by Arnaud et al. (1992). Recent XMM-Newton and Chandra observations have enabled us to study properties of the heavy elements in the ICM in detail. These observations showed not only Si and Fe, but also O and Mg abundance profiles, however the O and Mg abundance measurements have been limited only for the central regions of very bright clusters or groups of galaxies dominated by cD galaxies in a reliable manner (Finoguenov et al. 2002; Xu et al. 2002; Matsushita et al. 2003; Tamura et al. 2003; Buote et al. 2003a; Buote et al. 2003b; Humphrey & Buote 2006). Tamura et al. (2004) derived IMLR for five clusters, and the oxygen mass for several clusters with XMM-Newton. However, oxygen-mass-to-light ratios (OMLR) for rich clusters are not reliable due to the lower emissivity of O VII and O VIII lines in high temperatures. Matsushita et al. (2007b) showed different distribution profiles among the metals, which suggest difference in the process of metal enrichment. The abundance measurements of O and Mg with XMM-Newton, particularly for the outer regions of groups and clusters, are quite difficult due to the relatively high intrinsic background. Suzaku XIS can measure all the main elements from O to Fe, because it realizes lower background and higher spectral sensitivity, especially below 1 keV (Koyama et al. 2007). Matsushita et al. (2007a), Sato

et al. (2007a), Sato et al. (2008), and Tokoi et al. (2008) have shown the abundance profiles of O, Mg, Si, S, and Fe with Suzaku to the outer regions with good accuracy.

NGC 507 is a nearby group of galaxies ($z = 0.01646$) characterized by a smooth distribution of ICM. The ICM properties have been studied with ROSAT (Kim & Fabbiano 1995; Paolillo et al. 2003), ASCA (Matsumoto et al. 1997), Chandra (Kraft et al. 2004; Humphrey & Buote 2006; Rasmussen & Ponman 2007), and XMM-Newton (Kim & Fabbiano 2004). Kim & Fabbiano (1995) revealed a cooler central region with ROSAT PSPC, and Kim & Fabbiano (2004) showed the supersolar metal abundances within the D_{25} ellipse of NGC 507 with XMM-Newton. On the other hand, Humphrey & Buote (2006) showed a near solar metal abundances, the same as derived by Kraft et al. (2004) with Chandra. Kim & Fabbiano (2004) and Humphrey & Buote (2006) showed the α -elements to iron ratios, and both the abundance ratios were almost consistent to be ~ 1 solar. Kraft et al. (2004) also reported a sharp edge or a discontinuity in the radial surface brightness profile 55 kpc east and southeast of NGC 507 covering an $\sim 125^\circ$ arc. NGC 507 is also a known radio source and has been classified as an FR I radio galaxy (Fanti et al. 1986), and the edge of the radio lobe corresponds to the discontinuity of the X-ray surface brightness as shown in Kraft et al. (2004).

This paper reports on results from Suzaku observations of NGC 507 out to $13' \simeq 260 h_{70}^{-1}$ kpc, corresponding to $\sim 0.24 r_{180}$. We use $H_0 = 70 \text{ km s}^{-1} \text{ Mpc}^{-1}$, $\Omega_\Lambda = 1 - \Omega_M = 0.73$ in this paper. At a redshift of $z = 0.01646$, $1'$ corresponds to 20.1 kpc, and the virial radius, $r_{180} = 1.95 h_{100}^{-1} \sqrt{k\langle T \rangle} / 10 \text{ keV Mpc}$ (Markevitch et al. 1998), is 1.08 Mpc ($54'$) for an average temperature of $k\langle T \rangle = 1.5 \text{ keV}$. Throughout this paper we adopt the Galactic hydrogen column density of $N_H = 5.24 \times 10^{20} \text{ cm}^{-2}$ (Dickey & Lockman 1990) in the direction of NGC 507. Unless noted otherwise, the solar abundance table is given by Anders & Grevesse (1989), and the errors are in the 90% confidence region for a single interesting parameter.

2. Observations and Data Reduction

2.1. Observation

Suzaku observed the central region of NGC 507 in July 2006 (PI: K. Sato) with an exposure time of 79.6 ks. The observation log is given in table 1, and the XIS image in 0.5–4 keV is shown in figure 1. We analyze only the XIS data in this paper, although Suzaku observed the object with both XIS and HXD, which acquired the data. The XIS instrument consists of four sets of X-ray CCDs (XIS 0, 1, 2, and 3). XIS 1 is a back-illuminated (BI) sensor, while XIS 0, 2, and 3 are front-illuminated (FI). The instrument was operated in the Normal clocking mode (8 s exposure per frame), with the standard 5×5 or 3×3 editing mode.

It is known that the optical blocking filters (OBF) of the XIS have gradually been contaminated by outgassing from the satellite. The thickness of the contaminant is different among the sensors, and is also dependent on the location

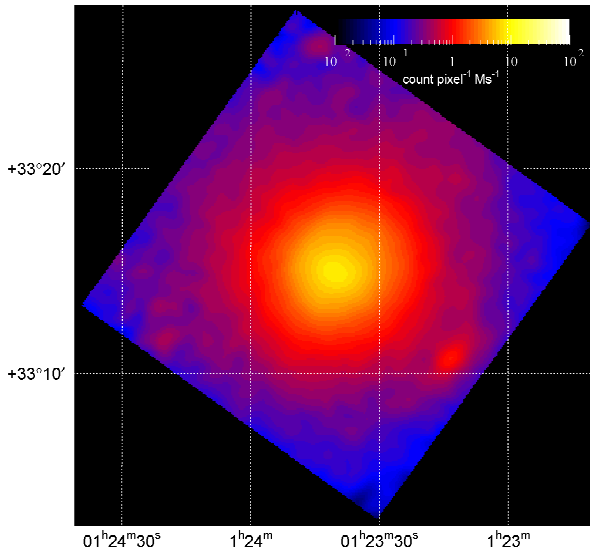


Fig. 1. Combined XIS image of central observation in the 0.5–4.0 keV energy range. The observed XIS0-3 images were added on the sky coordinate after removing each calibration source region, and smoothed with $\sigma = 16$ pixel $\simeq 17''$ Gaussian. Estimated components of extragalactic X-ray background (CXB) and instrumental background (NXB) were subtracted, and the exposure was corrected, though vignetting was not corrected.

Table 2. Estimated column density of the contaminant for each sensor at the center of CCD in units of 10^{18} cm^{-2} .

	XIS0	XIS1	XIS2	XIS3
Carbon	2.52	3.94	3.83	5.78
Oxygen	0.419	0.657	0.638	0.963

on the CCD chips in the way that it is thickest in the center. Estimated column densities (C/O=6 in number ratio is assumed) during the observation at the center of the CCD are given in table 2.¹ We included these effects in the calculation of the the Ancillary Response File (ARF) by the “xissimarfgen” ftools task of 2006-10-26 version (Ishisaki et al. 2007). Since the energy resolution also slowly degraded after the launch, due to radiation damage, this effect was included in the Redistribution Matrix File (RMF) by the “xisrmfgen” Ftools task of the 2006-10-26 version.

2.2. Data Reduction

We used version 1.2 processing data (Mitsuda et al. 2007), and the analysis was performed with HEASoft version 6.1.1 and XSPEC 11.3.2t. The analysis method was almost the same as those in Sato et al. (2007a) and Sato et al. (2008). However, because the observations were not supported by the Good-Time Intervals (GTI) defined to exclude the telemetry saturation by the XIS team, we

¹ Calibration database file of `ae_xiN_contami_20061024.fits` was used for the estimation of the XIS contamination ($N = 0, 1, 2, 3$ denotes the XIS sensor).

Table 1. Suzaku Observation logs for NGC 507.

Object	Seq. No.	Obs. date	(RA, Dec)* J2000	Exp. ksec	After screening (BI/FI) ksec
NGC 507	801017010	2006-07-28T14:51:16	(01 ^h 23 ^m 40 ^s 0, +33°15′21″)	79.6	79.2/79.2

* Average pointing direction of the XIS, written in the RA_NOM and DEC_NOM keywords of the event FITS files.

could not execute the GTI correction. The light curve of each sensor in the 0.3–10 keV range with a 16 s time bin was also examined in order to exclude periods with anomalous event rates which were greater or less than $\pm 3\sigma$ around the mean. After the above screenings, the remaining exposure time of the observation stayed almost unchanged as shown in table 1. The exposure after the screening was essentially the same as that before screening in table 1, which indicates that the non X-ray background (NXB) was almost stable during the observation. Event screening with cut-off rigidity (COR) was not performed in our data.

In order to subtract the NXB and the extra-galactic cosmic X-ray background (CXB), we employed the dark Earth database of 770 ks exposure, provided by the XIS team for the NXB, and employed the CXB spectrum given by Kushino et al. (2002). These analysis methods were also the same as in Sato et al. (2007a) and Sato et al. (2008). In order to remove influence from bright sources, we eliminated the regions within 80 arcsec from (01^h23^m14^s0, +33°10′57″) and within 45 arcsec from (01^h23^m39^s1, +33°09′04″) in our field of view. However, because the spatial resolution of Suzaku is not enough to resolve all point sources especially at the central region, effect from the remaining weaker point sources was taken into account in the spectral fitting function in the next sections.

2.3. Generation of ARFs

A precise surface brightness profile of NGC 507 was needed to generate the Suzaku ARF, and we used the XMM-Newton image which had much better spatial resolution than Suzaku. For this XMM-Newton data, we used MOS1+2 data (34.7 ks), and followed the data reduction by Sato et al. (2005). We subtracted blank-sky data as the background (Read & Ponman 2003), eliminated point sources in the ICM, and corrected the vignetting. Figure 2 shows a radial profile of NGC 507 with XMM-Newton in the 0.8–3 keV range, fitted with a β model. The origin of the profile is set at (RA, Dec) = (1^h23^m39^s7, +33°15′22″) in J2000.0. The best-fit parameters are $\beta = 0.48$ and $r_c = 1'.0$. Though the fit is not acceptable, the ARF showed little influence on the temperature and abundance in the spectral fits. We then generated two ARFs for the spectrum of each annular sky region, A^U and A^B , which respectively assumed uniform sky emission and $\sim 0.5^\circ \times 0.5^\circ$ size of the β -model surface brightness profile obtained with the XMM-Newton data. We did not use the raw XMM-Newton image, but the smoothed image derived from the parameters of the β -model fit to generate the ARFs, because the raw image had a gap between the CCD chips.

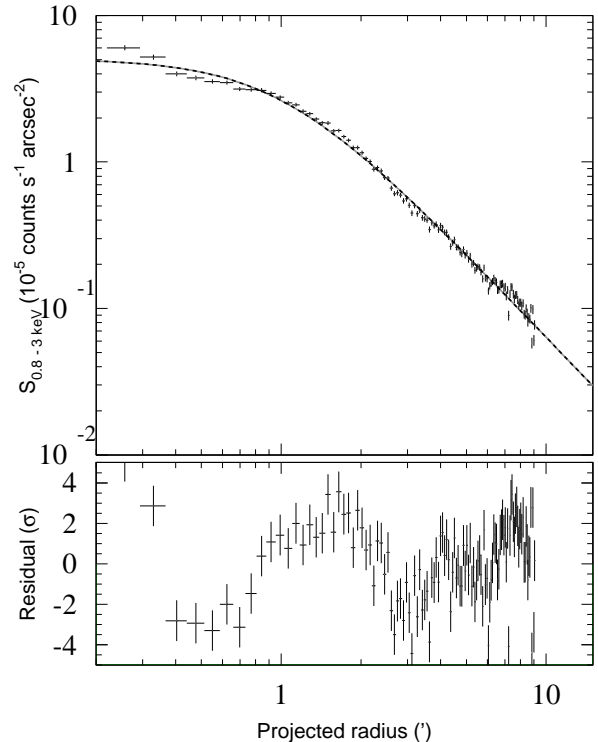


Fig. 2. In the upper panel, a radial profile of the surface brightness of NGC 507 in the 0.8–3 keV band is plotted for XMM-Newton MOS1+2 ($r < 10'$). The best-fit β model is shown by the solid gray line. In the bottom panel, the fit residuals are shown in units of σ , which correspond to the data minus the folded model, divided by 1σ error of each data point.

In this way, NGC 507 was characterized by a smooth and symmetric ICM distribution.

3. Temperature and Abundance Profiles

3.1. Spectral Fit

We extracted spectra from five annular regions of $0'-2'$, $2'-4'$, $4'-6'$, $6'-9'$, $r > 9'$, centered on (RA, Dec) = (1^h23^m40^s0, +33°15′21″). Table 3 lists the areas of the extracted regions (arcmin²), fractional coverage of the annulus (%), the SOURCE_RATIO_REG values (%; see caption for its definition) and the BI and FI counts for the observed spectra and the estimated NXB and CXB spectra. The fraction of the background, $f_{BGD} \equiv (\text{NXB} + \text{CXB})/\text{OBS}$, was less than $\sim 30\%$ even at the outermost annulus, although the Galactic component is not considered here. Each annular spectrum is shown in figure 3. The ionized Mg, Si, S, Fe lines are clearly seen in each

Table 3. Area, coverage of whole annulus, SOURCE_RATIO_REG, and observed/estimated counts for each annular region.

Region*	Area [†] (arcmin ²)	Coverage [†]	SOURCE_RATIO_REG [‡]	Energy (keV)	BI counts [§]				FI counts [§]			
					OBS	NXB	CXB	f_{BGD}	OBS	NXB	CXB	f_{BGD}
0'–2'	12.6	100.0%	29.2%	0.4–7.1	23,452	335	338	2.8%	49,445	509	794	2.6%
2'–4'	37.7	100.0%	21.9%	0.4–7.1	26,997	1,023	957	7.3%	53,622	1,501	2,284	7.1%
4'–6'	62.8	100.0%	14.4%	0.4–7.1	18,274	1,708	1,405	17.0%	34,960	2,488	3,356	16.7%
6'–9'	133.3	94.3%	13.4%	0.4–7.1	21,286	3,490	2,419	27.8%	38,891	4,961	5,520	26.9%
$r > 9'$	64.0	23.1%	4.0%	0.4–3.0	5,481	927	737	30.4%	9,420	1,218	1,497	28.8%

SOURCE_RATIO_REG represents the flux ratio in the assumed spatial distribution on the sky (β -model) inside the accumulation region to the entire model, and written in the header keyword of the calculated ARF response by “xissimarfgen”.

* The outermost region ($r > 9'$) include the calibration source region.

† The largest values among four sensors are presented.

‡ SOURCE_RATIO_REG \equiv COVERAGE $\times \int_{r_{\text{in}}}^{r_{\text{out}}} S(r) r dr / \int_0^{\infty} S(r) r dr$, where $S(r)$ represents the assumed radial profile of NGC 507, and we defined $S(r)$ in $30' \times 30'$ region on the sky.

§ OBS denotes the observed counts including NXB and CXB in 0.4–7.1 keV or 0.4–3 keV. NXB and CXB are the estimated counts.

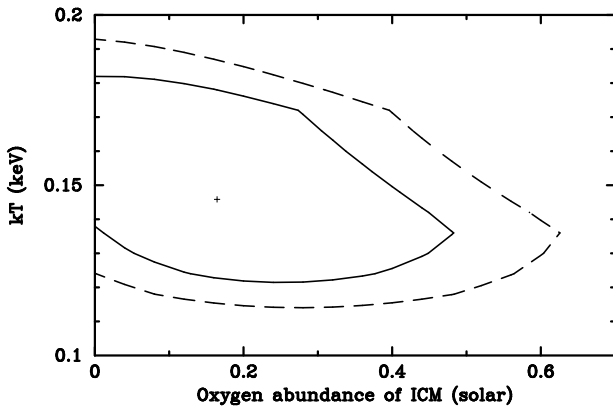


Fig. 4. A plot of confidence contour between kT of *apec* component (i.e. Galactic component) and the O abundance of *vapec* model (i.e. ICM) for the $r > 9'$ annulus, in the simultaneous fitting of all annuli with the *apec* + *phabs* \times (*vapec*₁ + *vapec*₂ + *zbremss*) model. The cross denotes the best-fit location, and the two contours represent 1σ and 90% confidence ranges, from inner to outer, respectively.

region. The O VII and O VIII lines are prominent in the outer rings, however, most of the O VII line is considered to come from the local Galactic emission, and we dealt with those in the same way as Sato et al. (2007a) and Sato et al. (2008).

The spectra from BI and FI for all regions were fitted simultaneously. For the four inner regions the fitted energy range was 0.4–7.1 keV, and it was 0.4–3.0 keV for the outermost region. In the simultaneous fit, the Galactic emission component as a background was common for all regions, while the NGC 507 emission component was unlinked between each region. We excluded the narrow energy band around the Si K-edge (1.825–1.840 keV) because of incomplete response. The energy range below 0.4 keV was also excluded because the C edge (0.284 keV) seen in the BI spectra could not be reproduced well in our data. The range above 7.1 keV was also ignored because Ni line (~ 7.5 keV) in the background left an artificial structure after the NXB subtraction at large radii. In the

simultaneous fit of BI and FI data, only normalization parameters were allowed to be different between them, although we found that the derived normalizations were quite consistent to be the same. For the outermost region ($r > 9'$) we fitted the spectrum in 0.4–3.0 keV to exclude contribution from the Fe-55 calibration source.

It is important to estimate the Galactic component precisely. In order to determine surface brightness and spectral shape of the Galactic component, we carried out simultaneous fit for all annuli. The Galactic component gives significant contribution in these annuli as shown in figure 3, however the ICM component is still dominant in almost all the energy range except for the O VII line.

We assumed either one or two temperature *apec* model for the Galactic component, and fitted the data with the following model formula: *apec*_{1T or 2T} + *phabs* \times (*vapec*_{1T or 2T} + *zbremss*). The resultant normalizations of the *apec* models in table 4 are scaled so that they give the surface brightness in the unit solid angle of arcmin², and the normalizations of the *apec* components were constrained to give the same surface brightness and the same temperature for all annuli. When we fitted the data with two *apec* models whose temperatures were free parameters, we could not obtain reasonable fit. Thus, we fixed the two temperatures to be 0.1 and 0.3 keV, which were consistent with the previous studies (e.g. Lumb et al. 2002). When we assumed two *apec* model, whose temperatures were fixed to be 0.1 and 0.3 keV, the resultant parameters were almost the same as those in table 5. As a result, we concluded that only one *apec* model was enough to fit the NGC 507 data since the fit improvement showed low significance with the two *apec* model. Therefore, we performed simultaneous fit in the 0.4–7.1 keV range (excluding 1.825–1.840 keV) for the four inner regions and in the 0.4–3.0 keV range for the $r > 9'$ region, assuming an *apec* model for the Galactic component, by following model, *apec* + *phabs* \times (*vapec*₁ + *vapec*₂ + *zbremss*), as shown in table 4.

To demonstrate how sensitive the O abundance of the ICM is to the assumed Galactic component model, we show in figure 4 a confidence contour between kT (keV) of the *apec* component and the O abundance (solar) of

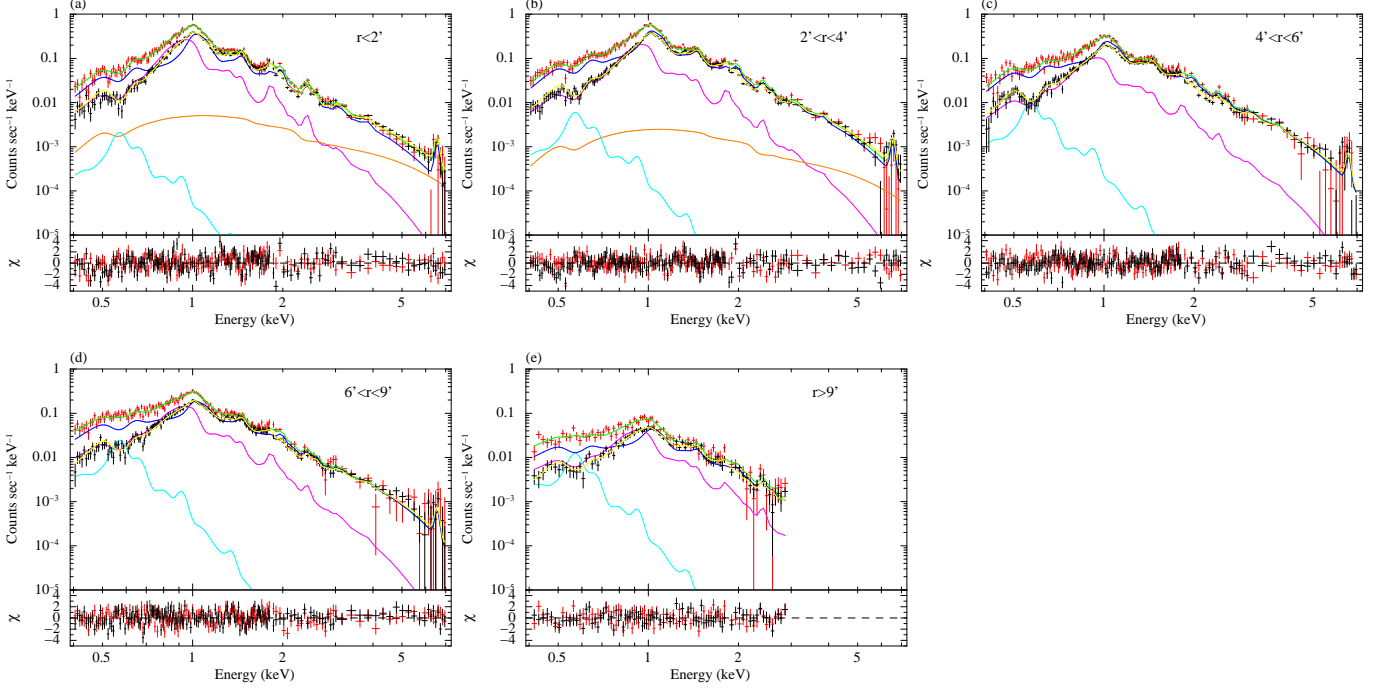


Fig. 3. The panels show the observed spectra at the annular regions of NGC 507 which are denoted in the panels, and they are plotted by red and black crosses for BI and FI, respectively. The estimated CXB and NXB components are subtracted, and they are fitted with the $apec + phabs \times (vapec_1 + vapec_2 + zbremss)$ model shown by green and yellow lines for the BI and FI spectra. The $vapec_1$ (hot) and $vapec_2$ (cool) components of ICM correspond to blue and magenta lines, respectively. The $apec$ component for the BI spectra are indicated by cyan line. The $zbremss$ component for the BI spectra within $r < 4'$ region are indicated by orange line. The energy range around the Si K-edge (1.825–1.840 keV) is ignored in the spectral fit. The lower panels show the fit residuals in units of σ .

Table 4. The best-fit parameters of the $apec$ component for the simultaneous fit of all spectra of NGC 507 with one or two temperature models ($apec$) for Galactic emissions and $phabs \times (vapec_{1T \text{ or } 2T} + zbremss_{r < 4'})$ model for ICM.

Fit model	$Norm_1^*$	kT_1 (keV)	$Norm_2^*$	kT_2	χ^2/dof
$apec_1 + phabs \times (vapec_1 + zbremss)$	0.47	0.110	–	–	3173/1520
$apec_1 + phabs \times (vapec_1 + vapec_2 + zbremss)$	0.42 ± 0.14	$0.159^{+0.034}_{-0.037}$	–	–	2067/1510
$apec_1 + apec_2 + phabs \times (vapec_1 + zbremss)$	0.26	0.1 (fix)	0.33	0.3 (fix)	3073/1520
$apec_1 + apec_2 + phabs \times (vapec_1 + vapec_2 + zbremss)$	1.02 ± 0.42	0.1 (fix)	0.13 ± 0.13	0.3 (fix)	2075/1510

* Normalization of the $apec$ component divided by the solid angle, Ω^u , assumed in the uniform-sky ARF calculation ($20'$ radius), $Norm = \int n_e n_H dV / (4\pi(1+z)^2 D_A^2) / \Omega^u \times 10^{-20} \text{ cm}^{-5} \text{ arcmin}^{-2}$, where D_A is the angular distance to the source.

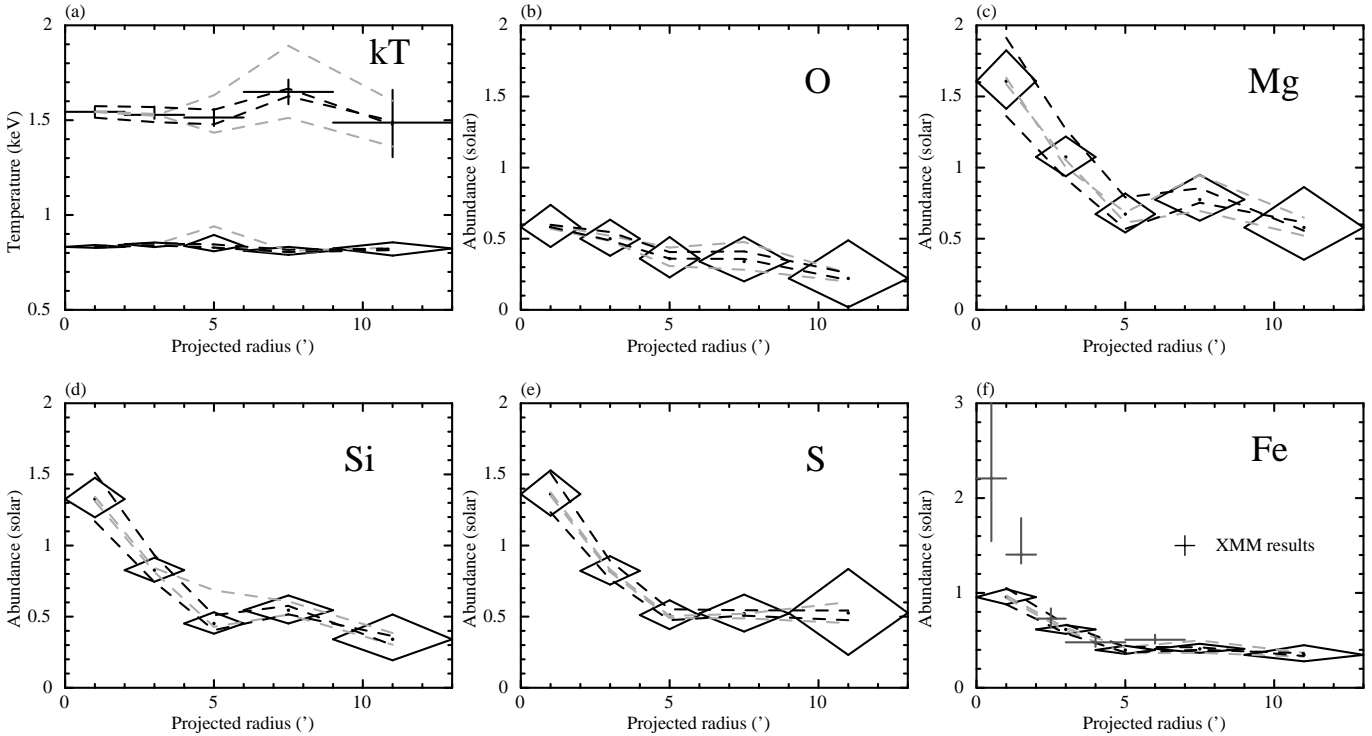


Fig. 5. (a): Radial temperature profiles derived from the spectral fit for each annulus against the projected radius. Black dashed lines show systematic change of the best-fit values by varying the thickness of the OBF contaminant by $\pm 10\%$. Light-gray dashed lines denote those when the estimated CXB and NXB levels are varied by $\pm 10\%$. (b)–(f): Radial abundance profiles derived and plotted in the same way as in (a). (f): XMM results of Fit 13 in Kim & Fabbiano (2004) correspond to gray crosses.

vapex for the outermost annulus ($r > 9'$). There seems a negative correlation between the two parameters, because higher temperature of the Galactic component produces more intense O VIII line relative to O VII one, which pushes to reduce the O VIII line from the ICM (*vapex* component). Influence on the derived temperature and abundance by the modeling of the Galactic component will be examined in subsection 3.2, too.

The ICM spectra for all regions were clearly better represented by two *vapex* models than one *vapex* model as shown in table 5. The abundances were linked in the following way, Mg=Al, S=Ar=Ca, Fe=Ni, and were also linked between the two *vapex* components for each region. The fit results are shown in table 5. Kim & Fabbiano (2004) showed that the model for the central region needed to include the low-mass X-ray binary (LMXB) component based on the ROSAT and XMM-Newton observations, we included a $kT = 7$ keV *zbrems* model for this component in the fit for 0–2' and 2–4' annuli. The resultant flux in 0.3–8 keV was $\sim 1 \times 10^{-13}$ and $\sim 4 \times 10^{-14}$ erg s $^{-1}$ cm $^{-2}$ for 0–2' and 2–4' region, respectively, and the flux due to the LMXB component with Suzaku was consistent with the Kim & Fabbiano (2004) result.

Although the fit was not statistically acceptable due mainly to the very high photon statistics compared with the systematic errors in the instrumental response, the results were useful to assess whether each element abundance was reasonably determined or not. Abundance of Ne was not reliably determined due to the strong and com-

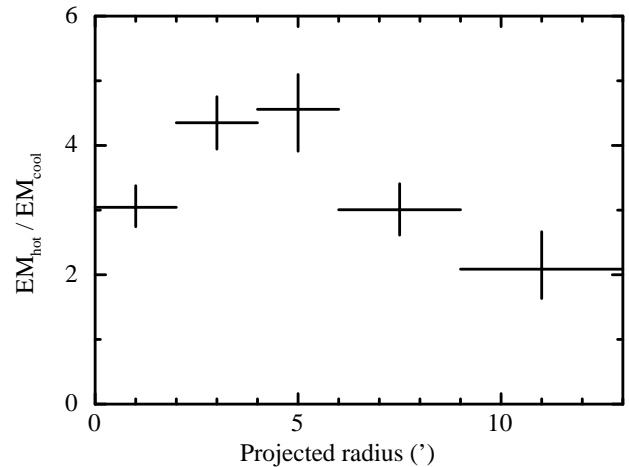


Fig. 6. The ratio of emission measure of the hot ICM component to that of the cool ICM component.

plex Fe-L line emissions, however we left these abundance to vary freely during the spectral fit.

Results of the spectral fit for each annulus are summarized in table 6 and figure 4, in which systematic error due to the OBF contamination and background (CXB + NXB) estimation are included. We examined the results by changing the background normalization by $\pm 10\%$, and the error range is plotted with light-gray dashed lines in figure 4. The systematic error due to the background es-

Table 5. Summary of the parameters from one or two *vap*ec fit (*ap*ec + *phabs* × (*vapec*_{1T or 2T} + *zbrems*_{*r*<4'})) to each annular spectrum of NGC 507. All annuli were simultaneously fitted. Errors are 90% confidence range of statistical errors, and do not include systematic errors. The solar abundance ratio of *angr* was assumed. These results are plotted in figure 5.

ICM1T	<i>Norm</i> ₁ *	<i>kT</i> ₁ (keV)	<i>Norm</i> ₂ *	<i>kT</i> ₂ (keV)	<i>Norm</i> ₁ / <i>Norm</i> ₂	χ^2/dof
0–2'	527.0	1.21	–	–	–	1118/339
2–4'	99.6	1.27	–	–	–	620/339
4–6'	29.0	1.26	–	–	–	560/340
6–9'	9.3	1.17	–	–	–	638/340
<i>r</i> > 9'	3.8	1.11	–	–	–	237/162
total						3173/1520
ICM1T	O (solar)	Ne (solar)	Mg,Al (solar)	Si (solar)	S,Ar,Ca (solar)	Fe,Ni (solar)
0–2'	0.23	0.00	0.25	0.31	0.40	0.22
2–4'	0.26	0.23	0.33	0.31	0.43	0.26
4–6'	0.35	0.05	0.56	0.55	0.63	0.42
6–9'	0.36	0.00	0.59	0.68	0.80	0.51
<i>r</i> > 9'	0.21	0.00	0.22	0.19	0.41	0.18
ICM2T	<i>Norm</i> ₁ *	<i>kT</i> ₁ (keV)	<i>Norm</i> ₂ *	<i>kT</i> ₂ (keV)	<i>Norm</i> ₁ / <i>Norm</i> ₂	χ^2/dof
0–2'	115.4 ± 7.0	1.54 ^{+0.02} _{-0.02}	38.0 ± 3.2	0.83 ^{+0.01} _{-0.01}	3.04 ± 0.32	576/337
2–4'	49.0 ± 2.8	1.53 ^{+0.04} _{-0.02}	11.3 ± 0.8	0.85 ^{+0.01} _{-0.01}	4.34 ± 0.39	436/337
4–6'	26.1 ± 1.7	1.51 ^{+0.05} _{-0.04}	5.7 ± 0.6	0.84 ^{+0.06} _{-0.03}	4.58 ± 0.57	469/338
6–9'	12.6 ± 0.9	1.65 ^{+0.06} _{-0.06}	4.2 ± 0.4	0.81 ^{+0.02} _{-0.02}	3.00 ± 0.36	399/338
<i>r</i> > 9'	8.5 ± 1.2	1.49 ^{+0.17} _{-0.18}	4.1 ± 0.8	0.82 ^{+0.03} _{-0.04}	2.07 ± 0.54	187/160
total						2067/1510
ICM2T	O (solar)	Ne (solar)	Mg,Al (solar)	Si (solar)	S,Ar,Ca (solar)	Fe,Ni (solar)
0–2'	0.58 ^{+0.16} _{-0.14}	2.02 ^{+0.41} _{-0.36}	1.61 ^{+0.22} _{-0.19}	1.33 ^{+0.15} _{-0.13}	1.36 ^{+0.17} _{-0.15}	0.96 ^{+0.09} _{-0.08}
2–4'	0.50 ^{+0.13} _{-0.12}	1.34 ^{+0.20} _{-0.20}	1.08 ^{+0.14} _{-0.14}	0.83 ^{+0.09} _{-0.08}	0.82 ^{+0.10} _{-0.10}	0.61 ^{+0.05} _{-0.05}
4–6'	0.36 ^{+0.15} _{-0.13}	1.00 ^{+0.28} _{-0.26}	0.67 ^{+0.15} _{-0.13}	0.45 ^{+0.08} _{-0.07}	0.51 ^{+0.10} _{-0.10}	0.40 ^{+0.05} _{-0.04}
6–9'	0.34 ^{+0.17} _{-0.14}	1.19 ^{+0.32} _{-0.29}	0.77 ^{+0.17} _{-0.15}	0.54 ^{+0.10} _{-0.10}	0.52 ^{+0.13} _{-0.13}	0.41 ^{+0.05} _{-0.04}
<i>r</i> > 9'	0.22 ^{+0.27} _{-0.20}	0.39 ^{+0.52} _{-0.39}	0.58 ^{+0.28} _{-0.23}	0.34 ^{+0.17} _{-0.15}	0.53 ^{+0.31} _{-0.29}	0.35 ^{+0.10} _{-0.07}

* Normalization of the *vap*ec component scaled with a factor of `SOURCE_RATIO_REG / AREA` in table 3, $Norm = \frac{\text{SOURCE_RATIO_REG}}{\text{AREA}} \int n_e n_H dV / [4\pi(1+z)^2 D_A^2] \times 10^{-20} \text{ cm}^{-5} \text{ arcmin}^{-2}$, where D_A is the angular distance to the source.

† All regions were fitted simultaneously.

timization is almost negligible. The other systematic error concerning the uncertainty in the OBF contaminant is shown by black dashed lines. A list of χ^2/dof is presented in table 6.

3.2. Temperature Profile

As mentioned in the previous section, the spectral fits needed two temperature model for ICM rather than one temperature model. As shown in table 5, the metal abundances changed dramatically whether we use one or two temperature models at the central region. Radial temperature profile and the ratio of the *vap*ec normalizations between the hot and cool ICM components are shown in figure 5(a) and figure 6, respectively. Our results for the two temperature ICM model are consistent with the XMM-Newton results (Kim & Fabbiano 2004) for the central region within 4'. In the Chandra case, Humphrey & Buote (2006) fitted the spectra with 1T model. The pre-

vious XMM-Newton and Chandra results neglected the Galactic component, while our analysis took it into account. We can crudely approximate the two temperatures as $kT_{\text{Hot}} \sim 1.5 \text{ keV}$, and $kT_{\text{Cool}} \sim 0.8 \text{ keV}$, respectively. The cool component is strongest in the innermost region, and even though it seems to decline in the outer regions, the possible coupling with the Galactic emission makes the precise estimation difficult. The radius of $10' \sim 200 \text{ kpc}$ corresponds to $\sim 0.19 r_{180}$, and the temperature decline, observed in several other clusters, is not clearly recognized in this system due partly to the multi-phase nature of ICM. The temperatures of cool and hot components are consistent with the results of two temperature model for NGC 5044 group with XMM-Newton in Buote et al. (2003a).

Systematic error caused by the background subtraction and by the estimation of the XIS filter contamination was estimated. We varied the sum of the NXB and

Table 6. List of χ^2/dof for each fit of NGC 507.

Region	nominal	contaminant		background	
		+10%	-10%	+10%	-10%
All	2067/1510	2004/1510	2148/1510	2104/1510	2094/1510

CXB flux and the contamination thickness individually by $\pm 10\%$. The results are shown by dashed lines in figure 5(a). Though kT_{cool} component is not affected by these uncertainties, kT_{Hot} shows a significant dependence on the background uncertainty most notably in the 6'–9' annulus. The tendency looks quite similar to the result for HCG 62 with Suzaku (Tokoi et al. 2008).

3.3. Abundance Profiles

Metal abundances are determined for the six element groups individually as shown in figures 5(b)–(f). O abundance is strongly affected by the Galactic emission as shown figure 4. However, the use of one or two temperature model for the Galactic emission did not significantly affect the abundance results as mentioned in subsection 3.1. We also note that Ne abundance has a problem in the spectral fit due to the coupling with Fe-L lines. Therefore, regarding the spatial structure, we dealt with the remaining four elemental groups: Mg, Si, S and Fe. The four abundance values and their variation with radius look quite similar to each other. The central abundances lie between 1.0–1.6 solar, and the abundance decline to about 1/5 of the central value is commonly seen in the $r > 9'$ annulus.

Kim & Fabbiano (2004) analyzed XMM-Newton data and employed the solar abundance by Grevesse & Sauval (1998) giving $[\text{Fe}/\text{H}] = 3.16 \times 10^{-5}$. This was scaled here by a factor of 0.7 to match the Anders & Grevesse (1989) value of $[\text{Fe}/\text{H}] = 4.68 \times 10^{-5}$. As shown in figure 5 (f), our result shows lower Fe abundance than the Kim & Fabbiano (2004) value within $r < 2'$, while both results are almost consistent in $2' < r < 5'$ region. The spectral model is the same for both analysis, employing the two temperature ICM model with the LMXB component. The difference is that our result was derived for the projected spectrum while Kim & Fabbiano (2004) used the deprojected spectra. The Fe abundance with Suzaku is also consistent with the Chandra result by Humphrey & Buote (2006). The resultant abundance profiles with Suzaku for NGC 507 are also consistent with those with the two temperature model for NGC 5044 with XMM-Newton in Buote et al. (2003b).

Again, we looked into the effect of the error by the NXB and CXB intensities and the OBF contamination. As shown by dashed lines in figures 5(b)–(f), the systematic effect is less than the statistical error for all regions.

3.4. Direct Comparison of O VII and O VIII Intensities

We examined the surface brightness of the O VII and O VIII emission lines in order to look into the origin of the O lines directly from the line intensities. The surface

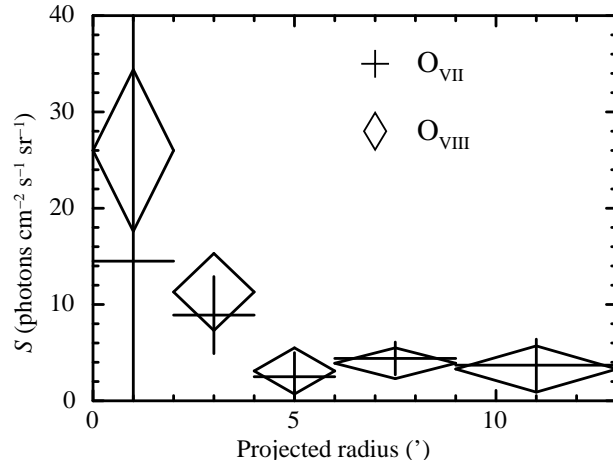


Fig. 7. Intensities of O VII and O VIII lines at each annulus of NGC 507 in units of photons $\text{cm}^{-2} \text{s}^{-1} \text{sr}^{-1}$. Numerical values are shown in table 7.

brightness of the lines was derived by fitting the annular spectrum with a *power-law + gaussian + gaussian* model. In this fit, we fixed the Gaussian σ to be 0, and allowed the energy center of the two Gaussians to vary within 555–573 eV or 648–658 eV for O VII or O VIII line, respectively. The derived line intensities are summarized in table 7 and figure 7. There is a clear excess of the O VIII intensity towards the cluster center, while O VII one is consistent to be constant. This is a clear evidence that the O VIII line is associated with the ICM itself, on the other hand, O VII may be due mainly to the Galactic origin.

4. Discussion

4.1. Metallicity Distribution in ICM

The present Suzaku observation of NGC 507 showed abundance distribution of O, Mg, Si, S, and Fe out to a radius of $13' \simeq 260$ kpc as shown in figure 5. Ne abundance has large ambiguity due to the strong coupling with Fe-L lines. Distributions of Mg, Si, S, and Fe are quite similar to each other, while O profile in the outer region has a large uncertainty. We plotted abundance ratios of O, Mg, Si, and S over Fe as a function of the projected radius in figure 8. The ratios Mg/Fe, Si/Fe and S/Fe are consistent to be a constant value around 1.5–2, while O/Fe ratio for the innermost region ($r < 2'$) is significantly lower around 0.6. In addition, the O/Fe ratio suggests some increase with radius.

Recent Suzaku observations have presented abundance profiles in several other systems: an elliptical galaxy NGC 720 (Tawara et al. 2008), the Fornax cluster and

Table 7. Intensities of O VII and O VIII lines for each annulus of NGC 507 field in units of photons $\text{cm}^{-2} \text{s}^{-1} \text{sr}^{-1}$. These intensities are derived from the spectral fit with the model *power-law + gaussian + gaussian*, assuming the uniform-sky ARF response. Results by McCammon et al. (2002) measured with a high resolution microcalorimeter array for a large sky area of $\sim 1 \text{ sr}$ are also presented.

Region	O VII	O VIII
NGC 507 (0–2′)	$14.5^{+82.8}_{-14.5}$	26.0 ± 8.4
NGC 507 (2–4′)	8.9 ± 4.0	11.3 ± 4.0
NGC 507 (4–6′)	2.5 ± 2.5	3.1 ± 2.4
NGC 507 (6–9′)	4.4 ± 1.7	3.9 ± 1.6
NGC 507 ($r > 9′$)	3.7 ± 2.7	3.3 ± 2.4
Galactic average (McCammon et al. 2002)	4.8 ± 0.8	1.6 ± 0.4

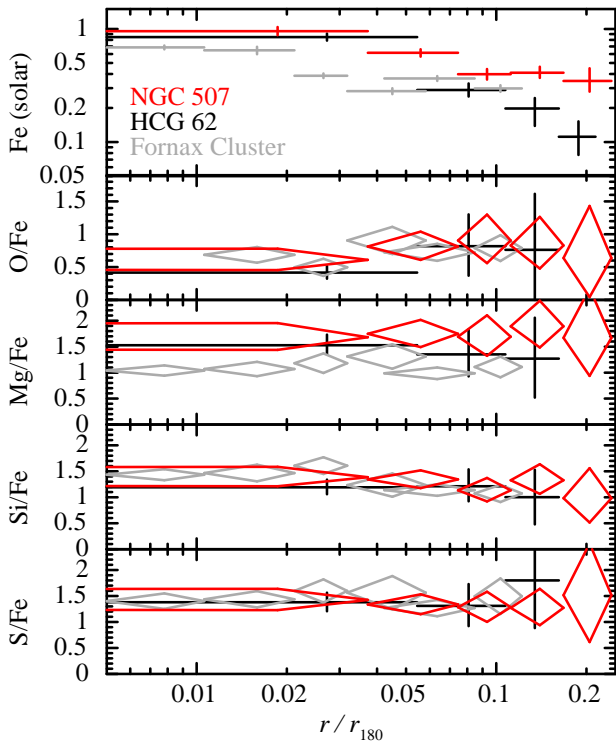


Fig. 8. Comparison of the abundance ratio for NGC 507 (red) with results for the HCG 62 group (black; Tokoi et al. 2008) and the Fornax cluster (gray; Matsushita et al. 2007b). Fe abundance and the O/Fe, Mg/Fe, Si/Fe, and S/Fe abundance ratios in solar units (Anders & Grevesse 1989) are plotted against the projected radius scaled by the virial radius, r_{180} , in all panels.

NGC 1404 (Matsushita et al. 2007b), and a cluster of galaxies Abell 1060 (Sato et al. 2007a) and AWM 7 (Sato et al. 2008). All systems show very similar value of Si/Fe ratio, to be 1–1.5. Mg/Fe ratio is slightly higher in HCG 62, Abell 1060 and AWM 7 than in other systems, i.e. NGC 720, Fornax cluster, and NGC 1404. We compare metal abundances of NGC 507 with those in the Fornax cluster and HCG 62 as shown in figure 8. The solar abundance by Feldman (1992), giving $[\text{Fe}/\text{H}] = 3.24 \times 10^{-5}$ and employed by Matsushita et al. (2007b), was scaled by a factor of 0.7 to match the Anders & Grevesse (1989) value. The Fe abundance of NGC 507 is almost the same as that of HCG 62 in the central region, while the Fornax cluster shows a lower value. Abundance ratios of O/Fe, Mg/Fe,

Si/Fe, and S/Fe are quite similar for these 3 systems at $r \sim 0.1 r_{180}$. Therefore, the abundance ratios show closer similarity than the absolute abundance values among different systems. The efficiency of the metal enrichment may depend on parameters such as age, starformation efficiency, contribution from cD galaxies. However, the relative contribution of SNe Ia and II and the process of metal mixing in the ICM seem to be quite similar for different clusters and groups.

Tamura et al. (2004) reported abundance ratios for 19 clusters studied with XMM-Newton, and the mean Si/Fe ratio in cool and medium temperature clusters with $kT < 6 \text{ keV}$ was ~ 1.4 . This is consistent with the Suzaku results for groups and poor clusters including NGC 507. Their O/Fe ratio, ~ 0.6 , in the cluster core also agrees with the Suzaku results including our NGC 507 case. Matsushita et al. (2003); Matsushita et al. (2007a) also reported abundance ratio for M87 and the Centaurus cluster, respectively, based on XMM-Newton observations. M87 showed Mg/O ratio to be ~ 1.3 in the central region, and the Centaurus cluster indicated O/Fe and Si/Fe ratios within $8′$ to be consistent with our results. The Si/Fe ratio for NGC 507 with XMM-Newton (Kim & Fabbiano 2004) and Chandra (Humphrey & Buote 2006) is ~ 1 , which is almost the same as our result.

Sato et al. (2007b) studied contributions of SNe Ia and II to the metal enrichment, based on Suzaku results of NGC 507, Abell 1060, AWM 7, and HCG 62 (Sato et al. 2007a; Sato et al. 2008; Tokoi et al. 2008). Sato et al. (2007b) showed the number ratios of SNe II to Ia to be ~ 3.5 for the ICM of the above systems. These results also suggest that the clusters and groups have passed the same metal enrichment process in the ICM.

4.2. Metal Mass-to-Light Ratio

We examined the parameter of metal mass-to-light ratios for oxygen, iron, and magnesium (OMLR, IMLR, and MMLR, respectively) to compare the ICM metal distribution with the stellar mass profile. The metal mass profiles shown in figure 9(a) were calculated from the 3-dimensional gas mass profile, which is based on the surface brightness profile by XMM-Newton (see also figure 2 and subsection), the gas density in the central region, $r < 2′$, through our spectral fit as shown in table 5, and the abundance profile measured with Suzaku. The derived iron, oxygen, and magnesium mass within the 3-dimensional

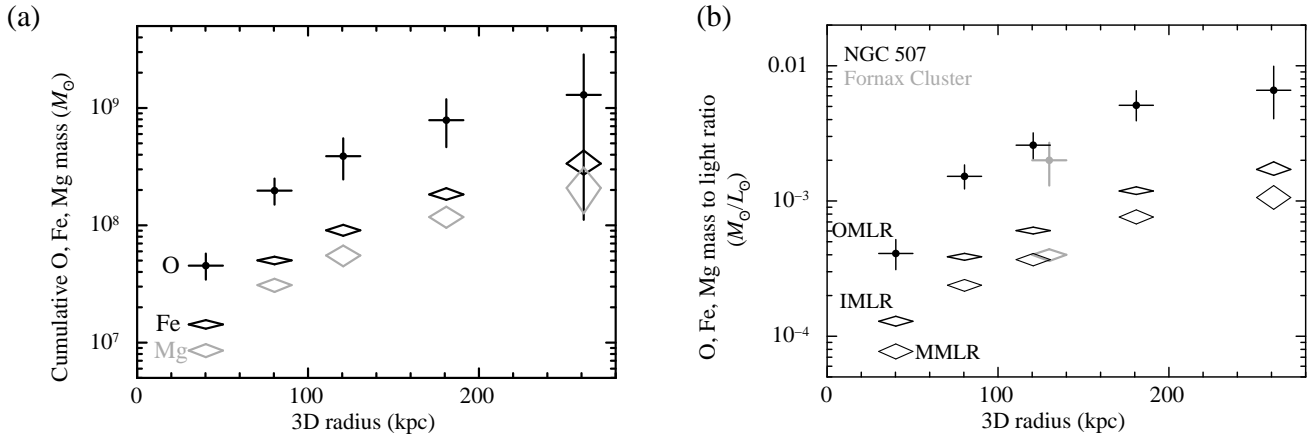


Fig. 9. (a) Cumulative mass, $M(< R)$, within the 3-dimensional radius, R , for O, Fe, and Mg in NGC 507, based on the combination of the abundance determination with Suzaku and the gas mass profile with XMM-Newton. (b) Ratio of the O, Fe, and Mg mass in units of M_{\odot} to the B band optical luminosity in units of L_{\odot} (OMLR, IMLR, and MMLR, respectively) against the 3-dimensional radius. Black symbols represent our results for NGC 507, and gray symbols of OMLR and IMLR are for the Fornax cluster by Matsushita et al. (2007b).

Table 8. Comparison of IMLR, OMLR and MMLR for all systems.

	IMLR	OMLR	MMLR	r (kpc/ r_{180})	$k(T)$	Reference
Suzaku						
NGC 720	1×10^{-4}	4×10^{-4}	–	25/0.04	~ 0.56 keV	Tawara et al. (2008)
Fornax	4×10^{-4}	2×10^{-3}	–	130/0.13	~ 1.3 keV	Matsushita et al. (2007b)
NGC 507	1.7×10^{-3}	6.6×10^{-3}	1.1×10^{-3}	260/0.24	~ 1.5 keV	This work
HCG 62	4.6×10^{-3}	3.8×10^{-2}	1.5×10^{-3}	230/0.21	~ 1.5 keV	Tokoi et al. (2008)
A 1060	4.0×10^{-3}	4.3×10^{-2}	1.6×10^{-3}	380/0.25	~ 3 keV	Sato et al. (2007a)
AWM 7	1.1×10^{-2}	5.8×10^{-2}	9.4×10^{-3}	570/0.35	~ 3.5 keV	Sato et al. (2008)
XMM-Newton						
Centaurus . . .	4×10^{-3}	3×10^{-2}	–	190/0.11	~ 4 keV	Matsushita et al. (2007a)

radius of $r < 260$ kpc are 3.4×10^8 , 1.3×10^9 , and 2.1×10^8 M_{\odot} , respectively.

Historically, B-band luminosity has been used for the estimation of the stellar mass (Makishima et al. 2001). We calculated the B-band luminosity in NGC507 by translation from the Two Micron All Sky Survey (2MASS)² with an appropriate color $B - K = 4.2$ for early-type galaxies in Lin & Mohr (2004), along with the Galactic extinction, $A_B = 0.267$, from NASA/IPAC Extragalactic Database (NED) in the direction of NGC 507. We used $2^{\circ} \times 2^{\circ}$ data set centered at the NGC 507 coordinate as shown in table 1, and subtracted the $r > 1^{\circ}$ region as a background, and also removed the NGC 499 region. In addition, we deprojected the luminosities along with the annuli of the spectral fits. The resultant luminosity within this Suzaku observation, $r < 13'$, is 2×10^{11} L_{\odot} in B-band. The radial luminosity profile corresponds to the value of figure 9 (a) divided by (b).

We calculated the integrated values of OMLR, IMLR, and MMLR within $r \lesssim 260$ kpc as shown in figure 9(b), and their values turned out to be $\sim 6.6 \times 10^{-3}$, $\sim 1.7 \times 10^{-3}$, and $\sim 1.1 \times 10^{-3}$ M_{\odot}/L_{\odot} , respectively. The errors are

only based on the statistical errors of metal abundance in the spectral fit, and the uncertainties of the gas mass profile and the luminosity of member galaxies are not included. The IMLR values are consistent with the collective results with ASCA by Makishima et al. (2001). The MMLR and IMLR show similar steep increase with radius up to $r \sim 150$ kpc and seem to reach almost a plateau at 150–300 kpc. This tendency is similar to the IMLR profile with XMM-Newton for M 87 and the Centaurus cluster by Matsushita et al. (2007a) within $r \lesssim 0.1 r_{180}$.

We also note that the derived OMLR and IMLR curves for NGC 507 in figure 9 are very similar to those for the Fornax cluster (Matsushita et al. 2007b) as seen in figure 9(b). We summarize recent measurements of IMLR and OMLR in table 8, where one can compare the present results with those in Fornax cluster, Centaurus cluster and NGC 720. It is suggested that smaller systems with lower gas temperature tend to show not only lower IMLR in Makishima et al. (2001) but also lower OMLR and MMLR, even though the scatter of the data is large. Because O and Mg are mainly synthesized by SNe II, while Fe is by both SNe Ia and II, as shown in Sato et al. (2007b), OMLR and MMLR show the ratios of heavy stars

² The database address: <http://www.ipac.caltech.edu/2mass/>

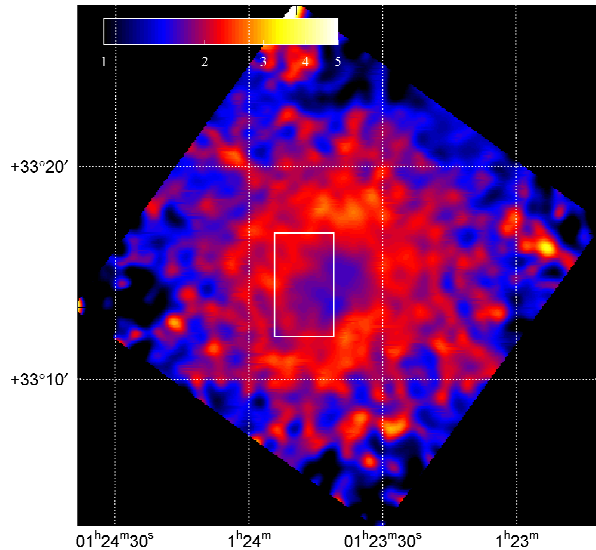


Fig. 10. Hardness ratio image for the two energy bands, 1–2 keV to 0.5–1 keV, in the central region of the Suzaku observation. The observed images by XIS0-3 were superposed on the sky coordinate after removing calibration source region, and smoothed with a Gaussian with $\sigma = 16$ pixel $\simeq 17''$. The white box corresponds to the X-ray discontinuity recognized by Kraft et al. (2004)

to galaxies. Although our observation within $r \lesssim 0.3 r_{180}$ show no clear difference between the distribution of IMLR and OMLR and MMLR, we need to observe the outer region to the virial radius in order to know the metal enrichment process of the ICM.

4.3. Discontinuity in the Surface brightness

Since previous X-ray observations suggested possible dynamical features in the NGC507 system (e.g. citekraft04), we looked into temperature structures which are out of axis symmetry in the form of 2-dimensional map of hardness ratio. Figure 10 shows the hardness ratio image based on the intensities in 1–2 keV and 0.5–1 keV. Although a vignetting correction was not performed, the two energy bands show very similar vignetting features. The transmission drop due to the OBF contamination was not corrected for either, which is larger for the 0.5–1 keV band and at the central part of the CCD image. Therefore, the hardness ratio should show a systematic drop from the center to the outer regions even for a constant temperature ICM. In the hardness image, the central region shows clearly lower hardness, and these feature is reported for HCG 62 observation in Tokoi et al. (2008). Including this feature, deviation from the circular symmetry is not significantly recognized in the hardness ratio image of NGC507.

Kraft et al. (2004) found a sharp edge or discontinuity in the X-ray surface brightness by Chandra in the east and south east region at $\sim 2'$ from the center. The discontinuity corresponds to the radius where the influence of the central cool component becomes weak, as indicated in

figure 10. Kraft et al. (2004) suggested three possibilities for the discontinuity; 1) the edge is caused by a motion of NGC 507 with respect to the larger scale dark matter potential of the group, 2) the pressure across the boundary is balanced by an unseen relic radio lobe produced in an earlier epoch of nuclear activity, 3) the discontinuity is created by the subsonic/transonic expansion of the relatively weak lobe currently observed lying interior to the discontinuity. Regarding the possibility 1, Kraft et al. (2004) noted that the temperatures inside and outside the discontinuity are almost the same. However, while Kraft et al. (2004) fitted with a single temperature model, we employed the two temperature model. As shown in figure 6 and 10, relative intensity of the cool component drops fairly sharply with radius around the discontinuity region.

Authors thank the referee for providing valuable comments. Part of this work was financially supported by the Ministry of Education, Culture, Sports, Science and Technology of Japan, Grant-in-Aid for Scientific Research Nos. 14079103, 15340088, 15001002, 16340077, 18740011, 19840043.

References

- Anders, E., & Grevesse, N. 1989, *Geochim. Cosmochim. Acta*, 53, 197
- Arnaud, M., Rothenflug, R., Boulade, O., Vigroux, L., & Vangioni-Flam, E. 1992, *A&A*, 254, 49
- Buote, D. A., Lewis, A. D., Brighenti, F., & Mathews, W. G. 2003, *ApJ*, 594, 741
- Buote, D. A., Lewis, A. D., Brighenti, F., & Mathews, W. G. 2003, *ApJ*, 595, 151
- Dickey, J. M., & Lockman, F. J. 1990, *ARA&A*, 28, 215
- Fanti, C., Fanti, R., de Ruiter, H. R., & Parma, P. 1986, *A&AS*, 65, 145
- Feldman, U. 1992, *Phys. Scr.*, 46, 202
- Finoguenov, A., David, L. P., & Ponman, T. J. 2000, *ApJ*, 544, 188
- Finoguenov, A., Arnaud, M., & David, L. P. 2001, *ApJ*, 555, 191
- Finoguenov, A., Matsushita, K., Böhringer, H., Ikebe, Y., & Arnaud, M. 2002, *A&A*, 381, 21
- Fukazawa, Y., Makishima, K., Tamura, T., Ezawa, H., Xu, H., Ikebe, Y., Kikuchi, K., & Ohashi, T. 1998, *PASJ*, 50, 187
- Fukazawa, Y., Makishima, K., Tamura, T., Nakazawa, K., Ezawa, H., Ikebe, Y., Kikuchi, K., & Ohashi, T. 2000, *MNRAS*, 313, 21
- Grevesse, N., & Sauval, A. J. 1998, *Space Science Reviews*, 85, 161
- Humphrey, P. J., & Buote, D. A. 2006, *ApJ*, 639, 136
- Ishisaki, Y., et al. 2007, *PASJ*, 59, 113
- Kim, D.-W., & Fabbiano, G. 1995, *ApJ*, 441, 182
- Kim, D.-W., & Fabbiano, G. 2004, *ApJ*, 613, 933
- Koyama, K., et al. 2007, *PASJ*, 59, 23
- Kraft, R. P., Forman, W. R., Churazov, E., Laslo, N., Jones, C., Markevitch, M., Murray, S. S., & Vikhlinin, A. 2004, *ApJ*, 601, 221
- Kushino, A., Ishisaki, Y., Morita, U., Yamasaki, N. Y., Ishida, M., Ohashi, T., & Ueda, Y. 2002, *PASJ*, 54, 327
- Lin, Y.-T., & Mohr, J. J. 2004, *ApJ*, 617, 879

- Lumb, D. H., Warwick, R. S., Page, M., & De Luca, A. 2002, *A&A*, 389, 93
- Makishima, K., et al. 2001, *PASJ*, 53, 401
- Markevitch, M., et al. 1998, *ApJ*, 503, 77
- Matsumoto, H., Koyama, K., Awaki, H., Tsuru, T., Loewenstein, M., & Matsushita, K. 1997, *ApJ*, 482, 133
- Matsushita, K., Finoguenov, A., Böhringer, H. 2003, *A&A*, 401, 443
- Matsushita, K., Böhringer, H., Takahashi, I., & Ikebe, Y. 2007b, *A&A*, 462, 953
- Matsushita, K., et al. 2007a, *PASJ*, 59, 327
- McCammon, D., et al. 2002, *ApJ*, 576, 188
- Mitsuda, K., et al. 2007, *PASJ*, 59, 1
- Mulchaey, J. S., Lubin, L. M., Fassnacht, C., Rosati, P., & Jeltama, T. E. 2006, *ApJ*, 646, 133
- Paolillo, M., Fabbiano, G., Peres, G., & Kim, D.-W. 2003, *ApJ*, 586, 850
- Rasmussen, J., & Ponman, T. J. 2007, *MNRAS*, 380, 1554
- Read, A. M., & Ponman, T. J. 2003, *A&A*, 409, 395
- Renzini, A. 1997, *ApJ*, 488, 35
- Renzini, A., Ciotti, L., D’Ercole, A., & Pellegrini, S. 1993, *ApJ*, 419, 52
- Sato, K., Furusho, T., Yamasaki, N. Y., Ishida, M., Matsushita, K., & Ohashi, T. 2005, *PASJ*, 57, 743
- Sato, K., et al. 2007a, *PASJ*, 59, 299
- Sato, K., Tokoi, K., Matsushita, K., Ishisaki, Y., Yamasaki, N. Y., Ishida, M., & Ohashi, T. 2007, *ApJL*, 667, L41
- Sato, K., Matsushita, K., Ishisaki, Y., Yamasaki, N. Y., Ishida, M., Sasaki, S., & Ohashi, T. 2008, *PASJ*, 60, S333
- Tamura, T., Kaastra, J. S., Makishima, K., & Takahashi, I. 2003, *A&A*, 399, 497
- Tamura, T., Kaastra, J. S., den Herder, J. W. A., Bleeker, J. A. M., & Peterson, J. R. 2004, *A&A*, 420, 135
- Tawara, Y., et al. 2008, *PASJ*, 60, S307
- Tokoi, K., et al. 2008, *PASJ*, 60, S317
- Xu, H., et al. 2002, *ApJ*, 579, 600